A projection-based approach to extend digital volume correlation for 4D spacetime measurements

Viktor Kosin, Amélie Fau, Clément Jailin, Benjamin Smaniotto, Thomas Wick, François Hild

Comptes Rendus
Mécanique

Draft

A projection-based approach to extend digital volume correlation for 4D spacetime measurements

Viktor Kosin [a, b], Amélie Fau [a], Clément Jailin [c], Benjamin Smaniotto [a], Thomas Wick [b, a] and François Hild [a]

[a] Université Paris-Saclay, CentraleSupélec, ENS Paris-Saclay, CNRS
LMPS–Laboratoire de Mécanique Paris-Saclay, Gif-sur-Yvette, France

[b] Leibniz Universität Hannover, Institut für Angewandte Mathematik (IFAM),
Hannover, Germany

[c] GE Healthcare, Buc, France

Abstract. *In-situ* (tomography) experiments are generally based on scans reconstructed from a large number of projections acquired under constant deformation of samples. Standard digital volume correlation (DVC) methods are based on a limited number of scans due to acquisition duration. They thus prevent analyses of time-dependent phenomena. In this paper, a modal procedure is proposed that allows time-dependent occurrences to be analyzed. It estimates spacetime displacement fields during the whole loading history. The spatial modes are based on standard DVC, which is subsequently enriched using projection-based digital volume correlation (P-DVC) to measure the temporal amplitudes. The method is applied to two cases, namely, a virtual experiment mimicking wedge splitting and an actual shear test on a pantographic metamaterial inducing large motions. With the proposed method, the temporal amplitude in the real test was measured for each projection leading to a temporal resolution of one tenth of a second and the analysis of 16,400 time steps. For the proposed algorithm, the sensitivity to the acquisition angle of the sample was investigated and measurement uncertainties were assessed.

Keywords. digital volume correlation (DVC), *in-situ* tests, spacetime analyses, tomography.

Funding. Financial support from the French-German University through the French-German Doctoral college "Sophisticated Numerical and Testing Approaches" (CDFA-DFDK 19-04) is acknowledged. This project was also partially supported by the French “Agence Nationale de la Recherche” through the “Investissements d’avenir” program (ANR-10-EQPX-37 MATMECA Grant).

This article is a draft

1. Introduction

X-ray computed tomography is an imaging technique that enables to reconstruct volumes of material absorption from series of projections [1, 2]. The developments of *in-situ* testing machines, which are placed inside X-ray scanners, give access to images of loaded samples [3]. The quantitative analysis of sample deformations may be assessed with Digital Volume Correlation (DVC) [4–6] with the measurement of displacement fields between discrete states. One significant limitation of such a procedure is the acquisition time of each scan. The reconstruction of a digital volume requires the sample to be steady during acquisitions of typically one thousand projections [3]. Depending on the imaging device, this acquisition may take few minutes up to few hours. This observation forbids *in-situ* experiments to image time-dependent phenomena such as creep or relaxation that occur when viscoelastic/viscoplastic materials are investigated. Furthermore, relaxation in *in-situ* experiments may result in motion artifacts. Currently, this is generally avoided by starting the acquisition of projections only after the measured force has stabilized [3, 7].

To circumvent the aforementioned restrictions, two routes are followed. First, fast scan acquisitions are carried out in synchrotron facilities with extremely bright X-ray beams [8, 9] using high-speed cameras [10, 11] at the expense of degraded reconstruction quality (due to blur induced by vibrations [10]). Another route consists in performing projection-based measurements leveraging the projection temporal sampling instead of their reconstruction. Compared to volume-based registration, the number of projections used to measure displacement fields in projection-based registrations can be reduced by typically three orders of magnitude [12–15],

which allows sub-minute *in-situ* experiments to be conducted in a lab scanner [16]. For such approaches, the spatial resolutions of the displacement fields are reduced [12, 15], a temporal regularization is introduced [14], or mechanical regularization is added to decrease the measurement uncertainties [13, 14].

In projection-based approaches, no standard DVC measurements were considered. This paper presents an enhanced DVC procedure by significantly increasing the temporal sampling of measured displacement fields. Thus, the spatial discretization of the displacement field is totally controlled by standard DVC procedures [6]. By acquiring on-the-fly projections during the loading phases between full scans, it is shown that it is possible to measure temporal amplitudes of the displacement field by projection-based registrations [12]. This method is essentially restricted to the number of frames a tomograph can acquire, which resulted in a temporal resolution of one tenth of a second in the present study. Following a continuous Galerkin finite element discretization in space [17], a discontinuous Galerkin discretization in time is developed such that the new method is compatible with standard practices of *in-situ* experiments and their analyses. By computing the displacement field at certain loading steps and not with a projection-based measurement strategy, the presented approach allows for high spatial resolutions *and* high temporal resolution while keeping the uncertainties low. Conceptually, a 4D spacetime framework is designed in which temporal and spatial components are formulated *simultaneously*. In modern numerical simulations, spacetime concepts and the corresponding discretizations are currently intensively investigated [18–20]. In projection-based DVC (P-DVC), 4D concepts were proposed as well by using proper generalized decomposition concepts [21, 22]. The following study introduces an alternative route constructing spatial modes via DVC, and then temporal modes via P-DVC. To this end, one of the goals is to formulate such 4D concepts within a spacetime setting.

The outline is as follows. In Section 2, the principle of the proposed procedure is presented by introducing the corresponding variational formulations of DVC and Projection-based DVC (P-DVC) methods, and formulating the sequential solution algorithm. The method is tested on a synthetic experiment and applied to a shear test on a pantographic metamaterial in Section 3.

2. Projection-enhanced DVC

2.1. *Spacetime framework*

The general aim of kinematic measurements is to determine how some material domain $\widehat{\Omega} \subset \mathbb{R}^3$ (or region of interest) deforms during time interval $[0, t_{\text{end}}]$, which forms the spacetime cylinder [18–20]. One is seeking a displacement field $\widehat{\mathbf{u}} : \widehat{\Omega} \times (0, t_{\text{end}}) \rightarrow \mathbb{R}^3$ that describes the change of the reference domain $\widehat{\Omega}$ to the deformed configuration $\Omega(t)$, such that

$$\Omega(t) = \left\{ \mathbf{x} = \widehat{\mathbf{x}} + \widehat{\mathbf{u}}(\widehat{\mathbf{x}}, t) : \widehat{\mathbf{x}} \in \widehat{\Omega}, t \in [0, t_{\text{end}}] \right\}, \tag{1}$$

where $\widehat{\mathbf{x}}$ denotes the position of any material point in the reference configuration $\widehat{\Omega}$, and $\mathbf{x}$ the position at time t. The displacement at spatial location $\mathbf{x} \in \Omega(t)$ is defined by

$$\mathbf{u}(\mathbf{x}, t) := \mathbf{x} - \widehat{\mathbf{x}} = \widehat{\mathbf{u}}(\widehat{\mathbf{x}}, t), \tag{2}$$

which completes the notations needed to describe the motion in Lagrangian and Eulerian frameworks.

A classical approach to measure $\widehat{\mathbf{u}}$ requires $\widehat{\Omega}$ and $\Omega(t)$ to be represented by a series of 3D images [4, 6, 23]

$$I : D \times [0, t_{\text{end}}] \rightarrow \mathbb{R}_{\geq 0}, \tag{3}$$

where $D \subset \mathbb{R}^3$ is the field of view, with $\Omega(t) \subset D$ for all $t \in [0, t_{\text{end}}]$. In practice, an image $I_t(\mathbf{x}) := I(\mathbf{x}, t)$ cannot be acquired instantaneously at time t (Figure 1). To reconstruct such an image by X-Ray computed tomography, hundreds if not thousands, of radiographs (i.e. projections) are needed over a full revolution (or turn) of the sample with respect to the detector [1].

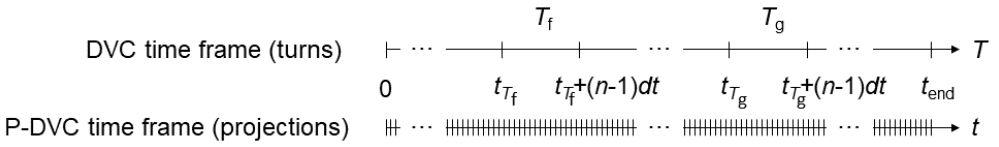

Figure 1. DVC and P-DVC temporal frames. In present case, n radiographs are acquired per turn. The temporal delay between two radiographic acquisitions is dt.

Conveniently, standard in-situ tomography experiments are designed to have phases when the loading is kept steady and the sample is rotated for one turn to acquire enough projections

for a full 3D reconstruction of volumes in deformed configurations [3]. These 3D images are no longer an instantaneous representation of the configuration $\Omega(t)$. Instead, they are reconstructed over the time needed for a turn T (Figure 1). To emphasize the different time scale, an image reconstructed from a set of radiographs acquired over a turn T is denoted by I_T. For displacement fields describing the 3D image I_T of the deformed configuration, capital letters will be used i.e. $\widehat{\mathbf{U}}(\widehat{\mathbf{x}}, T)$.

To measure the spacetime displacement field $\widehat{\mathbf{u}}$, separable variables are assumed. Hence, $\widehat{\mathbf{u}}$ is decomposed as

$$\widehat{\mathbf{u}}(\widehat{\mathbf{x}}, t) = \alpha(t)\widehat{\mathbf{W}}(\widehat{\mathbf{x}}), \tag{4}$$

with $\alpha : (0, t_{\text{end}}) \to \mathbb{R}$, and $\widehat{\mathbf{W}} : \widehat{\Omega} \to \mathbb{R}^3$. Let T_f and T_g be turns in $[0, t_{\text{end}}]$ with $T_f < T_g$, $\widehat{\mathbf{U}}(\widehat{\mathbf{x}}, T_f)$ and $\widehat{\mathbf{U}}(\widehat{\mathbf{x}}, T_g)$ the corresponding displacement fields, respectively, which are measured using standard DVC methods. Then, the space component of the displacement field is defined from DVC analyses as follows

$$\widehat{\mathbf{W}}(\widehat{\mathbf{x}}) = \widehat{\mathbf{U}}(\widehat{\mathbf{x}}, T_g) - \widehat{\mathbf{U}}(\widehat{\mathbf{x}}, T_f). \tag{5}$$

Having $\widehat{\mathbf{W}}(\widehat{\mathbf{x}})$ assessed, only the temporal amplitude $\alpha(t)$ is left unknown.

Remark 1. The freedom to choose T_f and T_g allows the displacement field to be computed at any point in time, before, after or even during reconstruction intervals. For example, when a sample is tested until failure, performing a final full scan is difficult, whereas it is simple to perform scans before and only acquire projections until failure to measure pre-failure displacement fields. A full acquisition of the initial state can also be challenging since the sample may need to be preloaded to ensure minimal motion for the first scan. Here one can exploit the fact that measurements are possible when $t < t_{T_f}$.

2.2. *Digital volume correlation*

As for most of the algorithms used for digital volume correlation, the conservation of gray levels of I is assumed. This hypothesis states that the gray level of each material point $\widehat{\mathbf{x}}$ is considered constant in time. Hence, for each image $I_{T_g}(\widehat{\mathbf{x}}) := I(\widehat{\mathbf{x}}, T_g)$ there is a displacement field $\widehat{\mathbf{U}}(\widehat{\mathbf{x}}, T_g)$ such that

$$I_{T_f}(\widehat{\mathbf{x}}) = I_{T_g}(\widehat{\mathbf{x}} + \widehat{\mathbf{U}}(\widehat{\mathbf{x}}, T_g)) \quad \forall \widehat{\mathbf{x}} \in \widehat{\Omega}, T_g \in [0, t_{\text{end}}], \tag{6}$$

where I_{T_f} is the image of the reference state, i.e. $\widehat{\mathbf{U}}(\widehat{\mathbf{x}}, T_f) \equiv \mathbf{0}$. Then, by considering another image $I_{T_g}(\widehat{\mathbf{x}})$ and applying decomposition (4) with condition (5), it follows that $\widehat{\mathbf{U}}(\widehat{\mathbf{x}}, T_g) = \widehat{\mathbf{W}}(\widehat{\mathbf{x}})$. Consequently, assumption (6) reads as follows. There is a displacement field $\widehat{\mathbf{W}}$ such that

$$I_{T_f}(\widehat{\mathbf{x}}) = I_{T_g}(\widehat{\mathbf{x}} + \widehat{\mathbf{W}}(\widehat{\mathbf{x}})) =: I_{T_g,\widehat{\mathbf{W}}}(\widehat{\mathbf{x}}) \quad \forall \widehat{\mathbf{x}} \in \widehat{\Omega}. \tag{7}$$

One seeks for a solution of the following minimization problem [24]. Find $\widehat{\mathbf{W}} \in \mathbb{V}(\widehat{\Omega}) := \mathbf{L}^2(\widehat{\Omega})$ such that

$$J_A(\widehat{\mathbf{W}}) = \inf_{\widehat{\mathbf{V}} \in \mathbb{V}(\widehat{\Omega})} J_A(\widehat{\mathbf{V}}) \quad \text{with} \quad J_A(\widehat{\mathbf{V}}) := \tfrac{1}{2} \| I_{T_f} - I_{T_g,\widehat{\mathbf{V}}} \|^2_{L^2(\widehat{\Omega})}. \tag{8}$$

Here, $\widehat{\mathbf{W}}$ is a solution to Equation (8) only if it fulfills the following first-order optimality condition

$$A(\widehat{\mathbf{W}})(\widehat{\mathbf{V}}) := \int_{\widehat{\Omega}} (I_{T_g,\widehat{\mathbf{W}}} - I_{T_f})(\widehat{\boldsymbol{\nabla}} I_{T_g,\widehat{\mathbf{W}}} \cdot \widehat{\mathbf{V}}) \, \mathrm{d}\widehat{\mathbf{x}} = \mathbf{0} \quad \forall \widehat{\mathbf{V}} \in \mathbb{V}(\widehat{\Omega}). \tag{9}$$

This is a nonlinear problem, and a Gauss-Newton scheme (see e.g. Ref. [25]) will be utilized for the minimization problem (9), the Hessian is needed

$$A'(\widehat{\mathbf{W}})(\delta\widehat{\mathbf{W}}, \widehat{\mathbf{V}}) = \int_{\widehat{\Omega}} (\widehat{\boldsymbol{\nabla}} I_{T_g,\widehat{\mathbf{W}}} \cdot \delta\widehat{\mathbf{W}})(\widehat{\boldsymbol{\nabla}} I_{T_g,\widehat{\mathbf{W}}} \cdot \widehat{\mathbf{V}}) + (I_{T_g,\widehat{\mathbf{W}}} - I_{T_f}) \, \delta\widehat{\mathbf{W}} \cdot (\widehat{\boldsymbol{\nabla}}^2 I_{T_g,\widehat{\mathbf{W}}}) \cdot \widehat{\mathbf{V}} \, \mathrm{d}\widehat{\mathbf{x}}. \tag{10}$$

This solution strategy is standard and explained in more details in Ref. [26].

2.3. *Projection-based digital volume correlation*

In the same spirit as the presented DVC framework, the underlying hypothesis of P-DVC is again the conservation of gray levels. Contrary to Equation (6), the problem is not stated in the Lagrangian framework, but in the Eulerian system [12]. With $I_{T_f}(\mathbf{x}) := I(\mathbf{x}, T_f)$, there is a displacement field $\mathbf{u}(\mathbf{x}, t)$ such that

$$I_{T_f,\mathbf{u}(t)}(\mathbf{x}) := I(\mathbf{x} - \mathbf{u}(\mathbf{x}, t), T_f) = I(\mathbf{x}, t) \quad \forall \mathbf{x} \in \Omega(t), t \in [0, t_{\text{end}}]. \tag{11}$$

Instead of assuming that there is another 3D image, only one projection is considered to be available for any considered time t. Let Π_θ be the linear projection operator of the underlying X-ray setup (Figure 2), which maps any 3D gray level image $I_t(\mathbf{x}) := I(\mathbf{x}, t)$ defined on the volume domain D to a 2D gray level image $\Pi_\theta[I_t]$ defined on the detector domain Ξ at angle $\theta(t) \in [0, 2\pi]$. Then, assuming Equation (11) holds, it follows that

$$\Pi_{\theta(t)}[I_{T_f,\mathbf{u}(t)}](\mathbf{r}) = \Pi_{\theta(t)}[I_t](\mathbf{r}) \quad \forall \mathbf{r} \in \Xi, t \in [0, t_{\text{end}}], \tag{12}$$

where $\mathbf{r}$ denotes a pixel coordinate defined on the detector plane Ξ. The projections acquired during an experiment are defined as

$$p_t(\mathbf{r},\theta(t)) := \Pi_{\theta(t)}[I_t](\mathbf{r}). \tag{13}$$

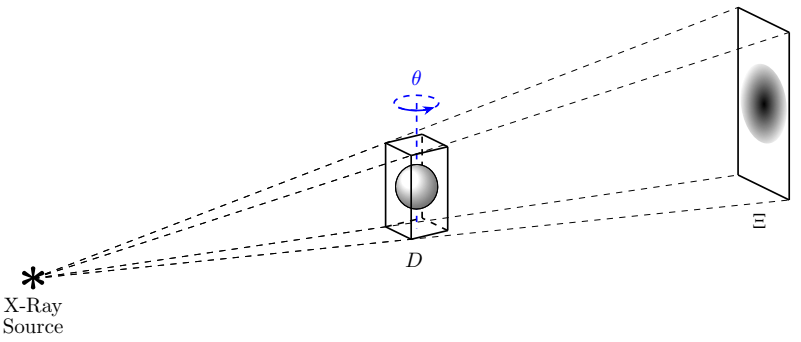

Figure 2. Schematic view of X-Ray Computed Tomography with a point source. A projection operator Π_θ maps the volume I_t defined on the domain D onto a 2D gray level image p_t defined on the detector plane Ξ.

Let $\omega(t) := \Pi_{\theta(t)}[\Omega(t)] \subset \Xi$ be the domain of the projection of $\Omega(t)$ at time t. Then, the gray level conservation assumption for the P-DVC problem is expressed as follows. There is a time-dependent amplitude $\alpha(t)$ such that

$$\Pi_{\theta(t)}[I_{T_f,\alpha,\mathbf{W}}](\mathbf{r}) = p_t(\mathbf{r},\theta(t)) \quad \forall \mathbf{r} \in \omega(t), t \in [0, t_{\text{end}}], \tag{14}$$

with

$$I_{T_f,\alpha,\mathbf{W}}(\mathbf{x}, t) := I_{T_f}(\mathbf{x} - \alpha(t)\mathbf{W}(\mathbf{x})). \tag{15}$$

Since $\widehat{\mathbf{W}}$ is computed using DVC and $\mathbf{W}(\mathbf{x}) = \widehat{\mathbf{W}}(\widehat{\mathbf{x}})$, only $\alpha(t)$ needs to be computed to assess $\mathbf{u}(\mathbf{x}, t)$. Consequently, the corresponding minimization problem consists in finding $\alpha \in \mathbb{Q} := L^2((0, t_{\text{end}}))$ such that

$$J_B(\alpha) = \inf_{\beta \in L^2((0,t_{\text{end}}))} J_B(\beta) \quad \text{with} \quad J_B(\beta) := \tfrac{1}{2}\|\Pi_{\theta(t)}[I_{T_f,\beta,\mathbf{w}}] - p_t\|^2_{L^2((0,t_{\text{end}});L^2(\omega(t)))}, \tag{16}$$

where the norm is defined as

$$\|\bullet\|^2_{L^2((0,t_{\text{end}});L^2(\omega(t)))} := \int_{(0,t_{\text{end}})} \int_{\omega(t)} \bullet^2 \, \mathrm{d}\mathbf{r} \, \mathrm{d}t. \tag{17}$$

This time, the corresponding optimality condition is given by

$$B(\alpha)(\beta) = \int_{(0,t_{\text{end}})} \int_{\omega(t)} \beta(\Pi_{\theta(t)}[I_{T_f,\alpha,\mathbf{W}}] - p_t)\Pi_{\theta(t)}[\boldsymbol{\nabla} I_{T_f,\alpha,\mathbf{W}} \cdot \mathbf{W}] \, \mathrm{d}\mathbf{r} \, \mathrm{d}t \stackrel{!}{=} 0, \qquad \forall \beta \in L^2((0,t_{\text{end}})). \tag{18}$$

To use again a Gauss-Newton scheme to solve this nonlinear problem, the Hessian is computed

$$B'(\alpha)(\delta\alpha,\beta) = \int_{(0,t_{\text{end}})} \int_{\omega(t)} \delta\alpha\beta\Pi_{\theta(t)}[\boldsymbol{\nabla} I_{T_f,\alpha,\mathbf{W}} \cdot \mathbf{W}]^2 + \delta\alpha\beta(\Pi_{\theta(t)}[I_{T_f,\alpha,\mathbf{W}}] - p_t)\Pi_{\theta(t)}[\mathbf{W} \cdot (\boldsymbol{\nabla}^2 I_{T_f,\alpha,\mathbf{W}}) \cdot \mathbf{W}] \mathrm{d}\mathbf{r} \, \mathrm{d}t. \tag{19}$$

Remark 2. In theory, the projected domain $\omega(t)$ and the projection p_t represent a projection of an image I_t of the deformed volume $\Omega(t)$. But I_t is not known. Further, $\Omega(t)$ is unknown as well, and thus $\omega(t)$. This feature has to be taken into account in the devised algorithm.

2.4. *Solution algorithm*

Summarizing the previous sections, two minimization problems are solved successively. For both minimization problems, a Gauss-Newton scheme is considered. The procedure is described in Algorithm 1.

Algorithm 1 P-DVC enhanced DVC algorithm

Choose an initial guess $\widehat{\mathbf{W}}^0$

Choose an initial guess α^0

while $\|\delta\widehat{\mathbf{W}}\| > TOL_{\widehat{\mathbf{W}}}$ **do** ▷ DVC minimization problem

Solve

$$A'(\widehat{\mathbf{W}}^l)(\delta\widehat{\mathbf{W}},\widehat{\mathbf{V}}) = -A(\widehat{\mathbf{W}}^l,\widehat{\mathbf{V}}) \quad \forall\widehat{\mathbf{V}}\in\mathbb{V} \tag{20}$$

$\widehat{\mathbf{W}}^{l+1} \leftarrow \delta\widehat{\mathbf{W}} + \widehat{\mathbf{W}}^l$

end while

$\mathbf{W}(\mathbf{x}) \leftarrow \widehat{\mathbf{W}}(\widehat{\mathbf{x}})$

while $\|u^l - u^{l-1}\| > TOL_u$ **do** ▷ P-DVC minimization problem

Approximate $\Omega(t)$ by

$$\Omega^l(t) \leftarrow \left\{\widehat{\mathbf{x}} + \widehat{\mathbf{u}}^l(\widehat{\mathbf{x}},t) : \widehat{\mathbf{x}}\in\widehat{\Omega};\ \widehat{\mathbf{u}}^l(\widehat{\mathbf{x}},t) = \alpha^l(t)\widehat{\mathbf{W}}(\widehat{\mathbf{x}})\right\}. \tag{21}$$

$\omega^l(t) \leftarrow \Pi_{\theta(t)}[\Omega^l(t)]$

Solve

$$B'(\alpha^l)(\delta\alpha,\beta) = -B(\alpha^l)(\beta) \quad \forall\beta\in\mathbb{Q} \tag{22}$$

$\alpha^{l+1} \leftarrow \alpha^l + \delta\alpha$

$\widehat{\mathbf{u}}^{l+1}(\widehat{\mathbf{x}},t) \leftarrow \alpha^{l+1}(t)\widehat{\mathbf{W}}(\mathbf{x})$

end while

Remark 3. In practice, the Hessians A' and B' given in Equations (10) and (19) are not exactly computed as they were defined, but only approximated by their first term. First, the second term is not always positive and therefore the Hessian itself could get indefinite. This could lead to a search direction that does not follow a descent direction. Second, it includes the Hessian of the current image, which itself is quite expensive to compute. To summarize, the two approximate Hessians read

$$A'(\widehat{\mathbf{W}})(\delta\widehat{\mathbf{W}},\widehat{\mathbf{V}}) \approx \int_{\widehat{\Omega}} (\widehat{\boldsymbol{\nabla}} I_{T_g,\widehat{\mathbf{W}}}\cdot\delta\widehat{\mathbf{W}})(\widehat{\boldsymbol{\nabla}} I_{T_g,\widehat{\mathbf{W}}}\cdot\widehat{\mathbf{V}})\,\mathrm{d}\widehat{\mathbf{x}} \tag{23}$$

and

$$B'(\alpha)(\delta\alpha,\beta) \approx \int_{(0,t_{\mathrm{end}})}\int_{\omega(t)} \delta\alpha\beta\Pi_{\theta(t)}[\boldsymbol{\nabla} I_{T_f,\alpha,\mathbf{W}}\cdot\mathbf{W}]^2\mathrm{d}\mathbf{r}\,\mathrm{d}t. \tag{24}$$

A detailed discussion about this point and other approximation approaches of the Hessian matrix is found in Ref. [27].

2.5. *Discretization*

The variational formulations (20) and (22) in the previous sections are not computationally accessible. Therefore Galerkin-type methods are introduced to solve the minimization problems in a numerical manner. In space, a finite-element discretization is defined on a tetrahedral discretization $\mathscr{T}_h$ of $\widehat{\Omega}$ with elements K and piecewise linear functions $\mathscr{P}_1$

$$\mathbb{V}_h(\widehat{\Omega}) := \left\{\mathbf{V}_h \in C(\widehat{\Omega}) \cap L^2(\widehat{\Omega}) : \mathbf{V}_h|_K \in \mathscr{P}_1 \text{ for all } K \in \mathscr{T}_h\right\}. \tag{25}$$

Let $\{\widehat{\mathbf{\Phi}}_i\}$ be the basis of $\mathbb{V}_h(\widehat{\Omega})$, then each element $\mathbf{V}_h \in \mathbb{V}_h(\widehat{\Omega})$ is of the form

$$\widehat{\mathbf{V}}_h(\widehat{\mathbf{x}}) = \sum_i a_i \widehat{\mathbf{\Phi}}_i(\widehat{\mathbf{x}}). \tag{26}$$

Then, the Galerkin ansatz (i.e. approximating partial differential equations in weak form using a finite-dimensional function space [28]) is used to replace Equation (20), and solve instead the following linear system

$$M^l_{ij} a_j = m^l_i, \tag{27}$$

with

$$M^l_{ij} = \int_{\widehat{\Omega}} (\widehat{\mathbf{\nabla}} I_{T_g,\widehat{\mathbf{w}}^l_h} \cdot \widehat{\mathbf{\Phi}}_j)(\widehat{\mathbf{\nabla}} I_{T_g,\widehat{\mathbf{w}}^l_h} \cdot \widehat{\mathbf{\Phi}}_i)\, \mathrm{d}\widehat{\mathbf{x}} \quad \text{and} \quad m^l_i = \int_{\widehat{\Omega}} (I_{T_f} - I_{T_g\widehat{\mathbf{w}}^l_h})(\widehat{\mathbf{\nabla}} I_{T_g,\widehat{\mathbf{w}}^l_h} \cdot \widehat{\mathbf{\Phi}}_i)\, \mathrm{d}\widehat{\mathbf{x}}. \tag{28}$$

In time, one wants to analyze each time step or more precisely each projection p_{t_k} separately. Hence, the interval $(0, t_{\text{end}})$ is subdivided into sub-intervals $(t_k - dt/2, t_k + dt/2)$ for $k = 1, ..., n_t$, and piecewise constant basis functions are selected. This decomposition results in the following (discontinuous) finite element space

$$\mathbb{Q}_h((0, t_{\text{end}})) := \left\{\beta_h \in L^2((0, t_{\text{end}})) : \beta_h(t)|_{(t_k - dt/2, t_k + dt/2)} = \text{const.},\ k = 1, ..., n_t\right\}. \tag{29}$$

As a basis of $\mathbb{Q}_h$, $\{\psi_k\}$ is chosen as

$$\psi_k(t) = \begin{cases} 1 & t \in (t_k - dt/2, t_k + dt/2), \\ 0 & \text{otherwise.} \end{cases} \tag{30}$$

This setting allows each element $\beta_h \in \mathbb{Q}_h$ to be written as

$$\beta_h(t) = \sum_k b_k \psi_k(t). \tag{31}$$

Last, instead of solving Equation (22), the following linear system is considered

$$N_{ij}^l b_j = n_i^l \tag{32}$$

with

$$\begin{aligned} N_{ij}^l &= \int_{(0,t_{\text{end}})} \int_{\omega^l(t)} \psi_j \psi_i \Pi_{\theta(t)} [\boldsymbol{\nabla} I_{T_f, \alpha_h^l, \mathbf{W}_h} \cdot \mathbf{W}_h]^2 \mathrm{d}\mathbf{r}\, \mathrm{d}t \\ n_i^l &= \int_{(0,t_{\text{end}})} \int_{\omega^l(t)} \psi_i (p_t - \Pi_{\theta(t)} [I_{T_f, \alpha_h^l, \mathbf{W}_h}]) \Pi_{\theta(t)} [\boldsymbol{\nabla} I_{T_f, \alpha_h^l, \mathbf{W}_h} \cdot \mathbf{w}_h]\, \mathrm{d}\mathbf{r}\, \mathrm{d}t. \end{aligned} \tag{33}$$

Remark 4. Assembling N_{ij} and n_i defined in Equation (33) is not straightforward. In a standard finite element code, one would simply choose some quadrature schemes. Without any preliminaries, this would require that one can select arbitrary quadrature points t_q in each interval $(t_k - dt/2, t_k + dt/2)$. Unfortunately one cannot evaluate p_t at any point in time, but only at the grid points t_k, as p_t is given by projections acquired during an experiment. In the present case, this issue is bypassed by having constant shape functions and using the midpoint rule for integration. Matrix [**N**] then becomes diagonal, such that each degree of freedom is solved independently and Equation (33) reduces to

$$b_i = \frac{n_i^l}{N_{ii}^l}. \tag{34}$$

One can freely choose the quadrature points when integrating over $\omega(t)$ or $\widehat{\Omega}$ by interpolating over the grid.

3. Application

In this section the proposed method is tested. First, only the projection-based Gauss-Newton scheme (Equations (21) and (22)) is applied to a synthetic experiment, where the displacement field $\widehat{\mathbf{W}}$ is predefined. Then, the complete algorithm is run on a real experiment. The ASTRA toolbox [29,30] was used for the cone beam projection operator Π and the DVC calculations were performed with the FE-based DVC library Correli 3.0 [31].

3.1. *Synthetic experiment*

For a first assessment of the proposed algorithm, a study of a predefined 3D image I_{T_f} of size $120 \times 90 \times 200$ vx (Figure 3) was performed.

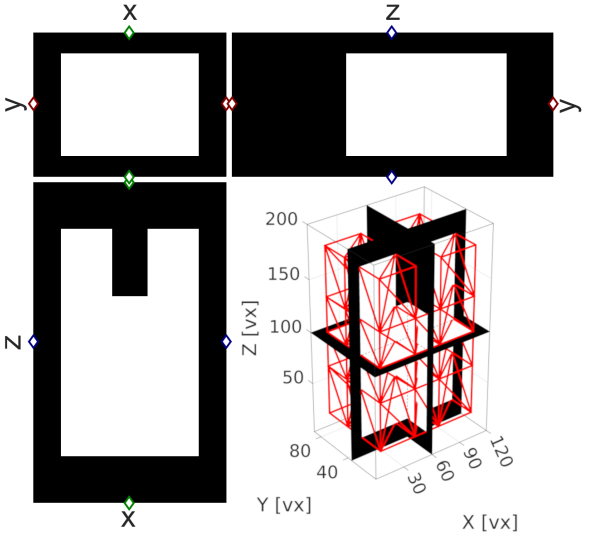

Figure 3. Sections of the phantom used in the synthetic experiment. The mesh is composed of 198 T4 elements whose mean volume is equal to 18^3 vx.

The sample $\widehat{\Omega}$ was bounded by a box of size $(L_x, L_y, L_z) = (85, 64, 141)$ vx and its gray levels were given by a uniform value

$$I_{T_f}|_{\widehat{\Omega}} \equiv 5 \cdot 10^{-3}. \tag{35}$$

The shape and motion of this synthetic case were inspired by wedge splitting tests [7], but for the sake of simplicity the sample did not rotate. The displacement field was chosen as

$$\widehat{\mathbf{u}}(\widehat{\mathbf{x}}, t) = \alpha(t)\widehat{\mathbf{W}}(\widehat{\mathbf{x}}), \tag{36}$$

where

$$\widehat{\mathbf{W}}(\widehat{\mathbf{x}}) = \frac{10}{L_z}(z-30)\frac{2}{L_x}(x-60.5)\,\widehat{\mathbf{e}}_x, \tag{37}$$

and

$$\alpha(t) = 3\tau^2 - 2\tau^3 \quad \text{with} \quad \tau = \frac{t}{t_{\text{end}}}, \tag{38}$$

with all spatial numbers expressed in voxels. The analytical displacement field $\widehat{\mathbf{W}}$ was chosen such that it was perfectly represented by the selected spatial finite element discretization (Figure 3); the convergence and accuracy should thus only be restricted to gray level interpolation or the projection algorithm. According to $\widehat{\mathbf{u}}$, defined by Equations (36-38), synthetically deformed images I_{t_k} were generated to compute projections p_k at times $\tau = 0, 1/4, ..., 1$, which are shown in Figure 4. The field is scaled such that at the final time step $t = t_{\text{end}}$ a maximum amplitude of about 10 vx was applied at the top of the sample, and no displacement at the bottom ($z = 30$ vx) during the whole test.

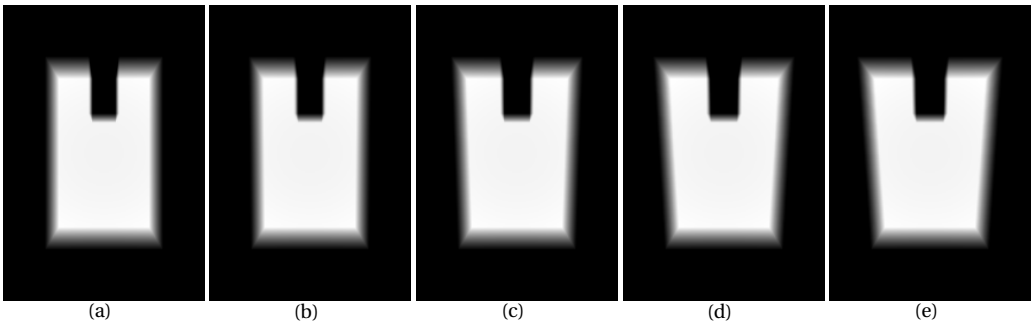

Figure 4. Artificial projections of the 3D image I_τ at dimensionless times (a) $\tau = 0$, (b) $\tau = 1/4$, (c) $\tau = 1/2$, (d) $\tau = 3/4$, (e) $\tau = 1$.

To validate the accuracy and speed of the computation of the temporal amplitude α with the proposed method, the absolute difference of the solution α and the computed amplitude α_h is presented in Figure 5(a). Since each amplitude was computed by minimizing the L^2-norm of the residuals ρ_t, the convergence of the root mean square (RMS) of the residuals is displayed in Figure 5(b). Even though no specific initialization was chosen for all projections (i.e. $\alpha^0(t_k) = 0$), the algorithm converged extremely fast, i.e. exponential convergence rates were reached for all time steps (Figure 5(a)), and with very low residuals (Figure 5(b)) essentially due to interpolation errors. The Newton solver converged after a maximum of 10 iterations to a tolerance of 10^{-9} in terms of amplitude corrections. A lower tolerance was not reached, because interpolation errors started to dominate the residual. For the last projection, this result indicates that the algorithm was not only fast but also robust for larger displacements (up to 10 vx in the present case).

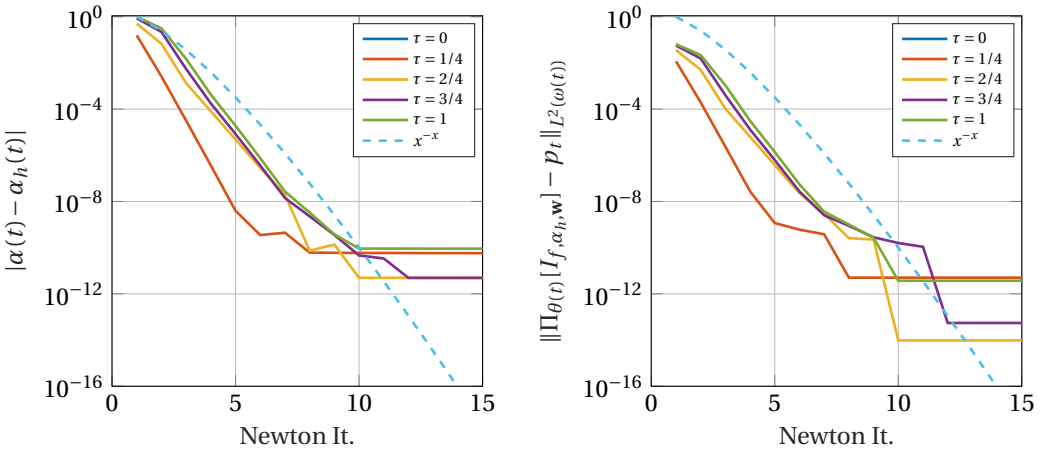

(a) (b)

Figure 5. Convergence of the amplitude α (a) and the projection (b) as functions of Newton iterations. The (cyan) dashed lines show that exponential convergence is reached.

3.2. *Shear test on pantographic metamaterial*

The proposed algorithm was also studied on an actual experiment. An *in-situ* shear test on a pantographic metamaterial, which was made of Polyamid PA2200 powder [32], was performed. The geometry of the sample is shown in Figure 6(b) and the pantographic structure was of size 105 mm × 35 mm × 45 mm. The sample, which was mounted horizontally in the *in-situ* tension-torsion-compression (TTC) testing machine (Figure 6(a)), was scanned in the North Star Imaging X50+ tomograph of LMPS at a binned definition (i.e. 1944 × 1536 pixels, see Table 1). The shear displacement was induced by clamping one side and pushing the other one down, such that a maximum stroke of 30 mm was reached at the end of the test (Figure 6(c)). The clamps were made of (3D printed) ABS and are visible in the reconstructed volumes as well as in the projections. Therefore, one has to take the motion of the clamps into account to have good results for the projection-based measurements. After flat-field corrections, the projections were further binned by a factor of four such that their final definition was 486 × 344 pixels, and the reconstructed volumes had a resolution of 372 µm per voxel. The reconstructions were performed with the simultaneous iterative reconstruction algorithm (SIRT) for cone beams [30]. In the reference configuration, the pantographic structure was in contact with the support. This contact zone

was not ideally meshed such that there the gray level assumption could not be fulfilled anymore (i.e. $I_{T_f,\hat{\mathbf{u}}_h}$ and $\Pi_{\theta(t)}[I_{T_f,\hat{\mathbf{u}}_h}]$ were only approximated). This phenomenon led to oscillations in α_h. To exclude these zones, $\Pi_{\theta(t)}[\Omega]$ was not chosen as the region of interest, but a slightly smaller subdomain of $\Pi_{\theta(t)}[\Omega]$ (Figure 9(a)).

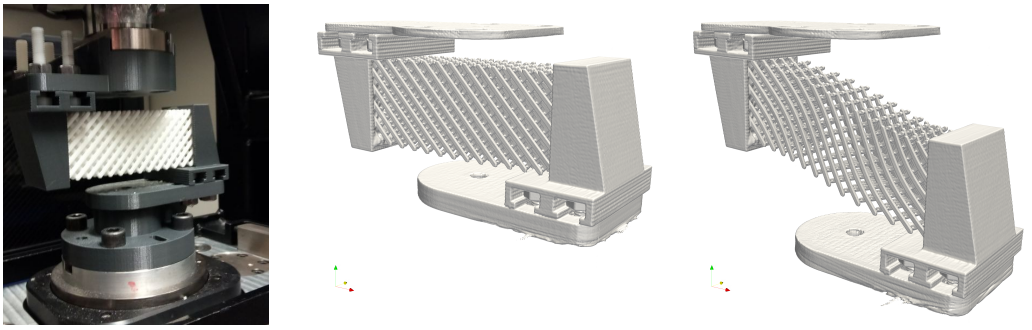

(a) (b) (c)

Figure 6. Sample inside the testing machine (a). Reconstructed volumes for scans 0 (b) and 3 (c).

The *in-situ* experiment protocol was devised as follows:

- The sample was turned continuously with a rotation speed of 3°/s during two revolutions, and 2,400 projections were simultaneously acquired at a rate of 10 fps (i.e. n = 1,200, and dt = 0.1 s). Scan 0 corresponds to the second turn.
- Then, the sample was loaded with a constant vertical stroke rate of 56 µm/s until a vertical displacement of 10 mm was reached while rotating at 3°/s for two more turns acquiring 1,200 projections per turn. Scan 1 corresponds to turn 6.
- The procedure was repeated until a maximum vertical displacement of 30 mm was reached considering 2 turns for each loading phase, and 2 turns for each stage with steady stroke.

The finite element mesh had 7,234 elements with an average volume of 18^3 vx (Figure 7).

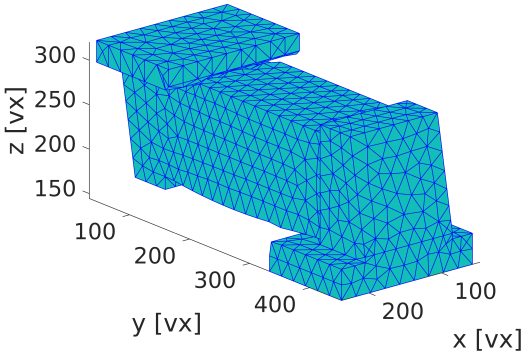

Figure 7. Finite element mesh used for the DVC analyses of the pantograph. The mean element volume is 18^3 vx.

For the analysis of the experiment, algorithm 1 was used with $TOL_{\mathbf{W}} = 10^{-3}$ vx and $TOL_u = 10^{-3}$ vx. As the solution strategy was decoupled (Remark 4), the minimization was performed for each projection separately. This separation allows the solution of the current projection to be used for the following one, such that convergence was reached after 7 iterations on average. The computation of each amplitude α took about one minute. In Figure 8 (a), the measured maximum vertical displacement is presented. One clearly sees the planned loading history with steady and loading phases. Due to continuous rotation of the sample, the projections were acquired at an increment of 0.3°, which resulted in visible fluctuations because not every angle of the sample was well suited for the registration procedure. For example, projections at some angles have more artifacts than others and the norm of the projected gradient is much lower such that they became more sensitive to acquisition noise.

Interestingly, the fluctuations did not increase over time and remained very low. The standard deviations of the amplitudes α during the turns for which the stroke was steady were equal to 7.4×10^{-3}, 8.7×10^{-3}, 7.7×10^{-3} and 7.1×10^{-3}), the corresponding standard deviations of the maximum displacement in the loading direction (i.e. u_z) were 0.20 vx, 0.23 vx, 0.21 vx and 0.19 vx, respectively.

Comparing the RMS of the projection residuals

$$\rho_t = \Pi_{\theta(t)}[I_{t,\alpha,\widehat{\mathbf{W}}}] - p_t \tag{39}$$

with the eigenvalue of the sensitivity B' (Equation (19)) at convergence (Figure 8(b)), it is observed that the angles for which the RMS residuals were high were associated with low values of the sensitivity and vice versa. This result indicates that the choice of the acquisition angle has an impact on the quality of the solution.

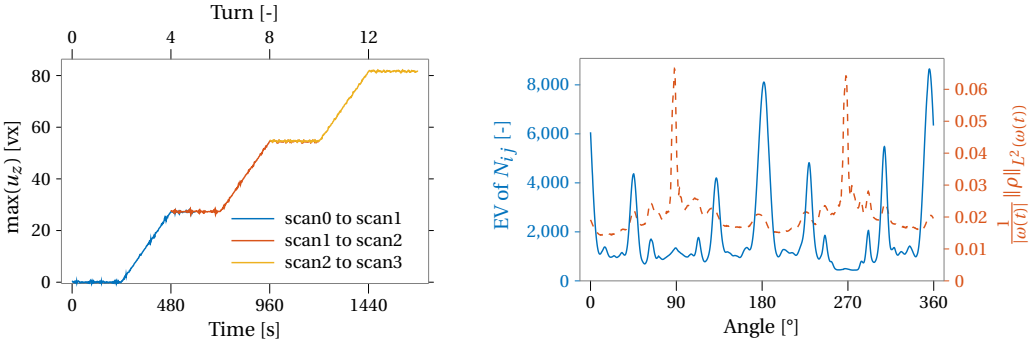

Figure 8. (a) Measured maximum vertical displacement u_z during the whole test. (b) Comparison of the angular eigenvalue (EV) of the Hessian matrix [**N**] and the RMS residual with respect to the angular position averaged over the first 6 revolutions (scans 0 to 1 analysis).

In Figure 9(a), one can see that the clamps are in front and behind the sample resulting in projections with low contrast. Yet, the residuals were low with respect to the dynamic range of the original radiographs even for angles that were not optimal (Figure 9(b-e)).

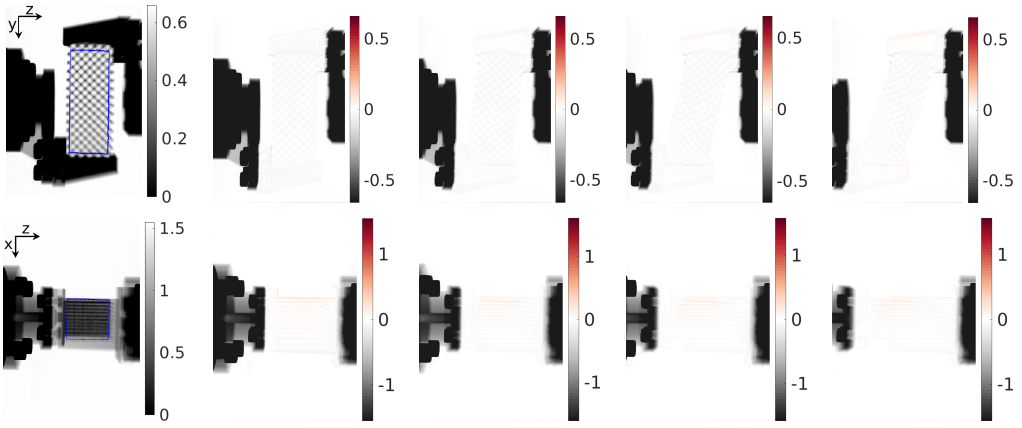

(a) (b) (c) (d) (e)

Figure 9. (a) Flat-field corrected projections with the region of interest ω (blue) at 0° (top) and 90° (bottom) angles. (b)-(e) Final residuals ρ for scans 0 to 3 for the 0° (top) and 90° (bottom) angles. The projections and final residuals are scaled by the maximum gray level in the region of interest ω.

The remaining residuals, visible in the zoomed view of scan 0 and scan 3 (Figure 10), show that the highest values are at the end of the beams of the pantograph. In these areas the macromesh, which was used for the analysis (Figure 7), was not able to match the kinematic details of the beams. Similar residuals were observed in the DVC analyses (for the same reasons).

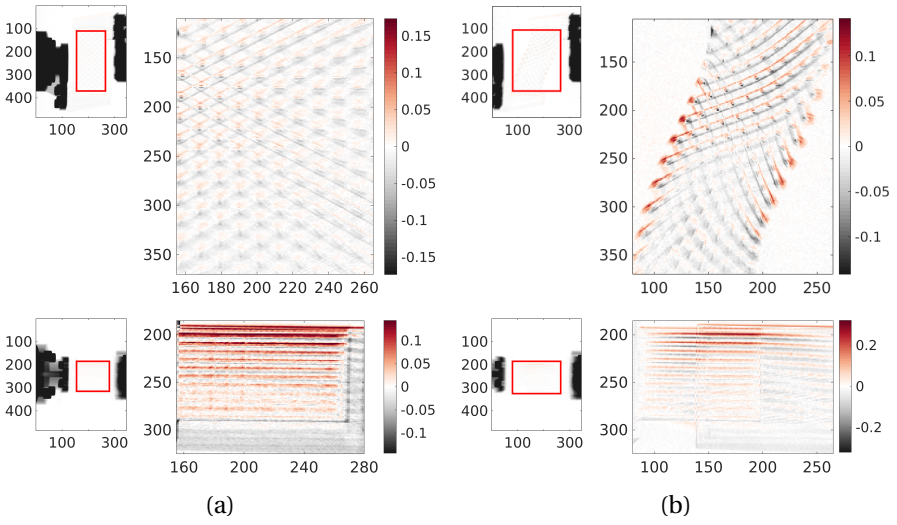

Figure 10. Zoomed view of the residuals ρ for scans 0 (a) and 3 (b). At the top are the 0° views and at the bottom the 90° views. The gray level color bar is scaled to the full dynamic range of the residuals inside the region of interest.

By comparing the maximum vertical displacement with the temporal history of the prescribed stroke of the testing machine (Figure 11(a)), it is concluded that there is a very good agreement between both signals. It is worth noting that the small differences (Figure 11(b)) were mostly dominated by a systematic angular error that already existed for turn 2, namely, the time interval corresponding to the reconstruction of the reference image. The measurements may be improved by further adjusting the geometrical parameters of the tomography setup. Another source for the error could be beam hardening. This effect was not corrected in the presented computations.

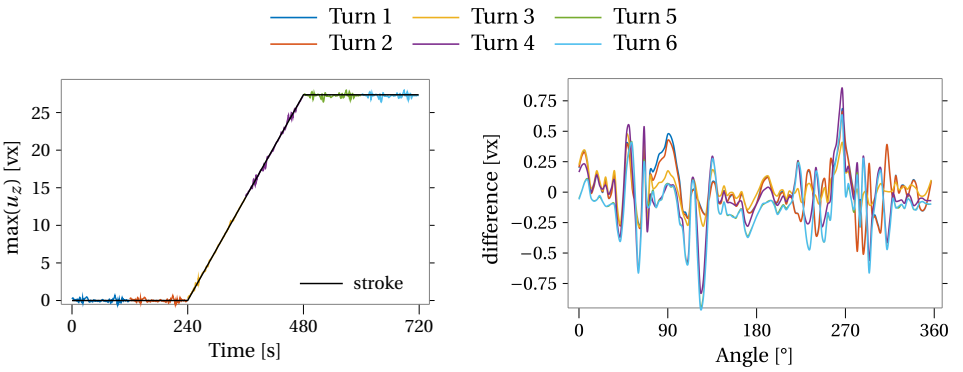

(a) (b)

Figure 11. (a) Measured maximum vertical displacement u_z for scans 0 to 1 compared to the prescribed stroke. (b) Difference between both signals for each turn.

4. Conclusion

A new spacetime framework was developed to measure 4D displacement fields by combining DVC and P-DVC. Using a spatiotemporal separation of variables, the computation of the spatial component (via DVC) was based on reconstructed volumes, and that of the temporal component (via P-DVC) on the projections acquired on-the-fly during the whole experiment.

By acquiring projections not only during a scan but also during the loading phase, it was possible to increase the temporal discretization of 4D measured displacement fields by more than three orders of magnitude (i.e. from 4 scans to 16,400 time steps) with projection-enhanced DVC. Since the choice of the acquisition angle had an impact on the quality of the solution, methods for choosing optimal angles are highly interesting and should be investigated. Yet, having already accurate results and the possibility of measuring a displacement of a volume at a speed of one tenth of a second indicated that the proposed methodology may help to measure real time-dependent phenomena such as, for example, viscous effects or crack propagation.

Conflicts of interest

The authors declare no competing financial interest.

Dedication

The manuscript was written through contributions of all authors. All authors have given approval to the final version of the manuscript.

Acknowledgments

The financial support of the French-German University through the French-German Doctoral college "Sophisticated Numerical and Testing Approaches" (CDFA-DFDK 19-04) is acknowledged. This project was also partially supported by the French “Agence Nationale de la Recherche” through the “Investissements d’avenir” program (ANR-10-EQPX-37 MATMECA Grant). Discussions are acknowledged within the framework of the International Research Training Group on Computational Mechanics Techniques in High Dimensions GRK 2657 funded by the German Research Foundation (DFG) under Grant Number 433082294.

References

[1] A. Kak, M. Slaney, Principles of Computerized Tomographic Imaging, Society of Industrial and Applied Mathematics, 2001.

[2] E. Maire, P. J. Withers, “Quantitative X-ray tomography”, International Materials Reviews **59** (2014), no. 1, p. 1-43.

[3] J. Buffière, E. Maire, J. Adrien, J. Masse, E. Boller, “In Situ Experiments with X ray Tomography: an Attractive Tool for Experimental Mechanics”, Experimental Mechanics **50** (2010), no. 3, p. 289-305.

[4] B. Bay, “Methods and applications of digital volume correlation”, Journal of Strain Analysis for Engineering Design **43** (2008), p. 745-760.

[5] M. Sutton, “Computer Vision-Based, Noncontacting Deformation Measurements in Mechanics: A Generational Transformation”, Applied Mechanics Reviews **65** (2013), no. AMR-13-1009, p. 050802.

[6] A. Buljac, C. Jailin, A. Mendoza, J. Neggers, T. Taillandier-Thomas, A. Bouterf, B. Smaniotto, F. Hild, S. Roux, “Digital Volume Correlation: Review of Progress and Challenges”, Experimental Mechanics **58** (2018), no. 5, p. 661-708.

[7] R. Vargas, R. Canto, B. Smaniotto, F. Hild, “Calibration of cohesive parameters for a castable refractory using 4D tomographic data and realistic crack path from in-situ wedge splitting test”, Journal of the European Ceramic Society **43** (2023), no. 2, p. 676-691.

[8] O. Ludwig, M. Dimichiel, L. Salvo, M. Suéry, P. Falus, “In-situ Three-Dimensional Microstructural Investigation of Solidification of an Al-Cu Alloy by Ultrafast X-ray Microtomography”, Metall. Mat. Trans. A **36** (2005), no. 6, p. 1515-1523.

[9] P. Lhuissier, M. Scheel, L. Salvo, M. Di Michiel, J. Blandin, "Continuous characterization by X-ray microtomography of damage during high-temperature deformation of magnesium alloy", Scripta Materialia **69** (2013), no. 1, p. 85-88.

[10] E. Maire, C. Le Bourlot, J. Adrien, A. Mortensen, R. Mokso, "20 Hz X-ray tomography during an in situ tensile test", International Journal of Fracture **200** (2016), p. 3-12.

[11] F. García-Moreno, P. Kamm, T. Neu, F. Bülk, R. Mokso, C. Schlepütz, M. Stampanoni, J. Banhart, "Using X-ray tomoscopy to explore the dynamics of foaming metal", Nature Communications **10** (2019), p. 3762.

[12] H. Leclerc, S. Roux, F. Hild, "Projection Savings in CT-based Digital Volume Correlation", Experimental Mechanics **55** (2015), no. 1, p. 275-287.

[13] T. Taillandier-Thomas, S. Roux, F. Hild, "Soft route to 4D tomography", Physical Review Letters **117** (2016), no. 2, p. 025501.

[14] C. Jailin, A. Bouterf, M. Poncelet, S. Roux, "In situ CT-scan Mechanical Tests: Fast 4D Mechanical Identification", Experimental Mechanics **57** (2017), p. 1327–1340.

[15] M. Khalili, S. Brisard, M. Bornert, P. Aimedieu, J.-M. Pereira, J.-N. Roux, "Discrete Digital Projections Correlation: a reconstruction-free method to quantify local kinematics in granular media by X-ray tomography", Experimental Mechanics **57** (2017), no. 6, p. 819-830.

[16] C. Jailin, A. Bouterf, R. Vargas, F. Hild, S. Roux, "Sub-minute in situ Fracture Test in a Lab CT-scanner", Integrating Materials and Manufacturing Innovation **8** (2019), p. 413-422.

[17] S. Roux, F. Hild, P. Viot, D. Bernard, "Three dimensional image correlation from X-Ray computed tomography of solid foam", Composites Part A: Applied Science and Manufacturing **39** (2008), no. 8, p. 1253-1265.

[18] U. Langer, O. Steinbach (eds.), Space-time methods: Application to Partial Differential Equations, volume 25 of Radon Series on Computational and Applied Mathematics, Berlin, de Gruyter, 2019.

[19] T. Wick, Space-time methods: formulations, discretization, solution, goal-oriented error control and adaptivity, https://thomaswick.org/links/Wi22_st_book_preprint_Dec_6_2022.pdf, to appear in Springer, Compact Textbooks in Mathematics, 2023.

[20] S. Larsson, R. Nochetto, S. Sauter, C. Wieners, "Space-time Methods for Time-dependent Partial Differential Equations", Oberwolfach reports **6** (2022), no. 1, p. 1-80.

[21] C. Jailin, A. Buljac, A. Bouterf, F. Hild, S. Roux, "Fast 4D tensile test monitored via X-CT: Single projection based Digital Volume Correlation dedicated to slender samples", Journal of Strain Analysis for Engineering Design **53** (2018), no. 7, p. 473-484.

[22] C. Jailin, A. Buljac, A. Bouterf, F. Hild, S. Roux, "Fast four-dimensional tensile test monitored via X-ray computed tomography: Elastoplastic identification from radiographs", Journal of Strain Analysis for Engineering Design **54** (2019), no. 1, p. 44-53.

[23] M. Sutton, J. Orteu, H. Schreier, Image correlation for shape, motion and deformation measurements: Basic Concepts, Theory and Applications, Springer, New York, NY (USA), 2009.

[24] R. Fedele, L. Galantucci, A. Ciani, "Global 2D digital image correlation for motion estimation in a finite ele-

ment framework: a variational formulation and a regularized, pyramidal, multi-grid implementation", International Journal for Numerical Methods in Engineering **96** (2013), no. 12, p. 739-762.

[25] P. Deuflhard, Newton Methods for Nonlinear Problems, Springer Series in Computational Mathematics, vol. 35, Springer Berlin Heidelberg, 2011.

[26] R. Fedele, A. Ciani, L. Galantucci, M. Bettuzzi, L. Andena, "A regularized, pyramidal multi-grid approach to global 3D-volume digital image correlation based on X-ray micro-tomography", Fundamenta Informaticae **125** (2013), no. 3-4, p. 361 – 376.

[27] J. Neggers, B. Blaysat, J. P. M. Hoefnagels, M. G. D. Geers, "On image gradients in digital image correlation", International Journal for Numerical Methods in Engineering **105** (2016), no. 4, p. 243-260.

[28] P. G. Ciarlet, The Finite Element Method for Elliptic Problems, Amsterdam ; New York : North-Holland Pub. Co. ; New York : Sole distributors for the U.S.A. and Canada, Elsevier North-Holland, 1978., 1978.

[29] W. van Aarle, W. J. Palenstijn, J. De Beenhouwer, T. Altantzis, S. Bals, K. J. Batenburg, J. Sijbers, "The ASTRA Toolbox: A platform for advanced algorithm development in electron tomography", Ultramicroscopy **157** (2015), p. 35-47, https://www.sciencedirect.com/science/article/pii/S0304399115001060.

[30] W. van Aarle, W. J. Palenstijn, J. Cant, E. Janssens, F. Bleichrodt, A. Dabravolski, J. D. Beenhouwer, K. J. Batenburg, J. Sijbers, "Fast and flexible X-ray tomography using the ASTRA toolbox", Opt. Express **24** (2016), no. 22, p. 25129-25147.

[31] H. Leclerc, J. Neggers, F. Mathieu, F. Hild, S. Roux, "Correli 3.0", IDDN.FR.001.520008.000.S.P.2015.000.31500, Agence pour la Protection des Programmes, Paris (France), 2015.

[32] F. dell'Isola, P. Seppecher, M. Spagnuolo, E. Barchiesi, F. Hild, T. Lekszycki, I. Giorgio, L. Placidi, U. Andreaus, M. Cuomo, S. Eugster, A. Pfaff, K. Hoschke, R. Langkemper, E. Turco, R. Sarikaya, A. Misra, M. De Angelo, F. D'Annibale, A. Bouterf, X. Pinelli, A. Misra, B. Desmorat, M. Pawlikowski, C. Dupuy, D. Scerrato, P. Peyre, M. Laudato, L. Manzari, P. Göransson, C. Hesch, S. Hesch, P. Franciosi, J. Dirrenberger, F. Maurin, Z. Vangelatos, C. Grigoropoulos, V. Melissinaki, M. Farsari, W. Muller, E. Abali, C. Liebold, G. Ganzosch, P. Harrison, R. Drobnicki, L. Igumnov, F. Alzahrani, T. Hayat, "Advances in Pantographic Structures: Design, Manufacturing, Models, Experiments and Image Analyses", Continuum Mechanics and Thermodynamics **31** (2019), no. 4, p. 1231-1282.

Appendix: Hardware parameters

The hardware parameters of the *in situ* setup are gathered in Table 1. Once cropped, the reconstructed volumes covered $180.6 \times 106.2 \times 146.4$ mm^3 with a 371 µm / vx resolution.

Table 1. DVC hardware parameters

Tomograph	North Star Imaging X50+
X-ray source	XRayWorX XWT-240-CT
Target / Anode	W (reflection mode)
Filter	none
Voltage	120 kV
Current	400 µA
Focal spot size	5 µm
Tube to detector	695.7 mm
Tube to object	430.9 mm
Detector	Dexela 2923
Definition	1536 × 1944 pixels (2 × 2 binning)
Number of projections	1200
Angular amplitude	360°
Frame average	1 per projection
Frame rate	10 fps
Acquisition duration	continous (1 turn lasted 2 min)
Reconstruction algorithm	SIRT
Gray Levels amplitude	16 bits
Volume size	486 × 286 × 394 vx (after crop)
Field of view	$180.6 \times 106.2 \times 146.4$ mm^3 (after crop)
Image scale	371 µm / vx